Monthly Notices of the ROYAL ASTRONOMICAL SOCIETY

MNRAS **528,** 7123–7136 (2024) https://doi.org/10.1093/mnras/stae362
Advance Access publication 2024 February 8

A radio flare associated with the nuclear transient eRASSt J234403−352640: an outflow launched by a potential tidal disruption event

A. J. Goodwin [1]★ G. E. Anderson [1] J. C. A. Miller-Jones [1] A. Malyali [2] I. Grotova,[2] D. Homan,[3] A. Kawka [1] M. Krumpe,[3] Z. Liu[2] and A. Rau[2]

[1]*International Centre for Radio Astronomy Research – Curtin University, GPO Box U1987, Perth, WA 6845, Australia*
[2]*Max-Planck-Institut für extraterrestrische Physik, Giessenbachstrasse 1, D-85748 Garching, Germany*
[3]*Leibniz-Institut für Astrophysik Potsdam, An der Sternwarte 16, D-14482 Potsdam, Germany*

Accepted 2024 February 1. Received 2024 January 30; in original form 2023 September 28

ABSTRACT

We present an extensive radio monitoring campaign of the nuclear transient eRASSt J234402.9−352640 with the Australia Telescope Compact Array, one of the most X-ray luminous TDE candidates discovered by the SRG/eROSITA all-sky survey. The observations reveal a radio flare lasting >1000 d, coincident with the X-ray, UV, optical, and infrared flare of this transient event. Through modelling of the 10 epochs of radio spectral observations obtained, we find that the radio emission is well-described by an expanding synchrotron emitting region, consisting of a single ejection of material launched coincident with the optical flare. We conclude that the radio flare properties of eRASSt J234402.9−352640 are consistent with the population of radio-emitting outflows launched by non-relativistic tidal disruption events, and that the flare is likely due to an outflow launched by a tidal disruption event (but could also be a due to a new AGN accretion event) in a previously turned-off AGN.

Key words: radio continuum: transients – transients: tidal disruption events – keyword3.

1 INTRODUCTION

The release of gravitational energy when mass is suddenly accreted onto a black hole powers some of the most explosive phenomena in the Universe. Most galactic nuclei host a supermassive black hole (Soltan 1982, SMBH), which can power highly energetic outflows from accretion events. Tidal disruption events are an extreme example of this process, occurring when a star passes too close to a supermassive black hole and is pulled apart by strong tidal forces (e.g. Hills 1975; Rees 1988). Approximately 50 per cent of the stellar material is initially bound to the black hole and accretes at rates approaching or surpassing the Eddington limit over a short (∼yrs) time-scale, with energy being fed back into the surrounding galaxy via outflows and radiation. Extreme variability and flaring events can also be caused by a sudden enhancement in a more persistent accretion flow onto a SMBH powering an active galactic nucleus (AGN; Rees 1984), with AGN flaring behaviour thought to be due to sudden accretion episodes or magnetic field changes (e.g. de Vries & Kuijpers 1992; Ciotti & Ostriker 2007; Hovatta et al. 2008). Therefore, the observational signatures of AGN flares and TDEs are similar as they are likely driven by the same process of a sudden increase in accretion rate onto the SMBH, although differences in the evolution of the accretion rate and circumnuclear environment may affect the evolution of the flare in each case.

Following the stellar disruption during a TDE, the bound material is thought to be the source of observed optical and X-ray emission (e.g. van Velzen et al. 2020), while the unbound, ejected material is thought to produce synchrotron emission from shocks with the surrounding circumnuclear medium (CNM), detected at radio wavelengths (e.g. Alexander et al. 2020). The first observed TDE candidates were discovered by the ROSAT All Sky Survey (Truemper 1982) as luminous ($10^{41–44}$ erg s^{-1}) X-ray outbursts with extremely soft ($\Gamma > 3$) X-ray spectra in galaxies that had no previous AGN activity (e.g. Komossa & Bade 1999; Donley et al. 2002). Optically-discovered TDEs radiate much of their energy in the optical/UV band (e.g. van Velzen et al. 2021) showing thermal blackbody emission with temperatures of $\sim 10^4$ K (Gezari et al. 2009; van Velzen et al. 2020), although, when discovered at wavelengths other than optical/UV can be optically dim (e.g. Mattila et al. 2018; Saxton et al. 2020; Malyali et al. 2023b). Many TDE optical light curves decay at early times broadly consistent with a $t^{-5/3}$ decay, appearing to trace the theoretical rate of mass fall back for complete disruptions (Phinney 1989; Guillochon & Ramirez-Ruiz 2013). There is a growing population of TDEs with unusual late-time optical behaviour, including rebrightenings (Hammerstein et al. 2023; Yao et al. 2023). Thermal X-rays are detected only in some events, with the X-ray rise potentially significantly delayed from the initial optical flare (e.g. Kajava et al. 2020). The X-ray decay phases can be highly non-monotonic (see discussion in Malyali et al. 2023b), in contrast with the relatively smoothly-declining optical light curves. It has been argued that the diversity of observational properties in TDEs is due to the varying mass, type, density, or structure of the star that is disrupted, varying black hole mass and spin, the orbit of the disrupted star, the host galaxy properties (including the presence of a pre-existing accretion disc), and the viewing angle (Lodato, King &

★ E-mail: ajgoodwin.astro@gmail.com

Pringle 2009; Guillochon & Ramirez-Ruiz 2015; Dai et al. 2018; Liu et al. 2023; Wevers et al. 2023; Malyali et al. 2023a).

Radio emission in TDEs is associated with synchrotron emission from outflowing material shocking the CNM of the host galaxy (see Alexander et al. 2020, for a review). Currently, the outflow mechanism is unknown but has been proposed to be accretion-powered jets or winds (e.g. Alexander et al. 2016; Stein et al. 2021; Cendes et al. 2022; Ravi et al. 2022; Somalwar et al. 2022, 2023), collision induced outflows (e.g. Lu & Bonnerot 2020a; Goodwin et al. 2023b), or the unbound debris stream (e.g. Krolik et al. 2016; Spaulding & Chang 2022). Recent radio observations of TDEs are illuminating a population of events that produce prompt radio-emitting outflows well described by synchrotron emission from material ejected at the time of the stellar disruption impacting the CNM (Alexander et al. 2016; Stein et al. 2021; Goodwin et al. 2022, 2023a,b). A number of TDEs have shown a late-time radio flare up to 1000s of days after the initial optical flare, thought to be due to the late launching of a mildly relativistic jet (Horesh, Cenko & Arcavi 2021; Cendes et al. 2022, 2023).

AGN also exhibit variability across the electromagnetic spectrum, including multiwavelength flares (Hovatta et al. 2008; Farrar & Gruzinov 2009) thought to be due to enhancements in accretion onto the SMBH (Ciotti & Ostriker 2007), magnetic energy release (de Vries & Kuijpers 1992), disc instabilities (Lightman & Eardley 1974; Sniegowska et al. 2020), and at radio frequencies shocks in the existing radio jet (Marscher & Gear 1985). Apparent AGN variability at radio frequencies may also be associated with interstellar scintillation or jet evolution (Ross et al. 2021). The link between variable optical and radio emission in AGN flares is not well studied. Two scenarios exist for producing an optical flare during an AGN radio flare: the first is due to a sudden increase in the mass being accreted, which could precede a radio flare by up to years depending on how and where the shock develops (Pyatunina et al. 2007). Alternatively, an optical flare may be observed directly related to a shock in the radio jet, as the optically thin tail of the shock spectrum may be detectable up to optical frequencies (Valtaoja et al. 1992a). Flaring AGN are usually observed to show continuous variability over decades of monitoring (Hovatta et al. 2008).

In this work, we present the discovery of a large-amplitude radio flare associated with the nuclear transient event eRASSt J234402.9−352640 (hereafter J2344). J2344 was first discovered on 2020 November 28 by the eROSITA instrument (Predehl et al. 2021) on-board the SRG observatory (Sunyaev et al. 2021) as a bright (0.2–2 keV $\log(L_X) \sim 44.7$), transient, ultra-soft X-ray source in the second eROSITA all-sky survey (Homan et al. 2023). The nucleus of the galaxy WISEA J234402.95−352641.8, at a redshift of $z = 0.1$, brightened by a factor of at least 150 in the 0.2–2 keV X-ray band, 3 mag in optical, and 0.3 mag in the infrared, with the first X-ray detection occurring ∼20 d after the optical peak (Homan et al. 2023). Follow-up optical spectra taken within weeks of the X-ray and optical flare show a blue continuum, broad Balmer emission lines and narrow [O III] and [N II] emission lines. Homan et al. (2023) analysed the early-time X-ray and optical characteristics of this transient event and found the most likely explanation for the transient emission to be a TDE within a turned-off AGN. However, they could not rule out a rapid increase in accretion in an AGN as an explanation, given the available observations.

Here, we present detailed, multi-epoch radio observations of J2344, in which we discovered transient radio emission associated with the event. In Section 2, we describe the observations and data reduction. In Section 3, we present the results and detailed spectral and equipartition modelling of the outflow properties. In Section 4, we describe the outflow properties and how they give insight into the nature of the outflow that was observed. In Section 5, we discuss the implications of the results and compare the observed properties of the transient with TDEs and AGN. Finally, in Section 6, we summarize the results and provide concluding remarks.

Table 1. Summary of ATCA observations of eRASSt J234402.9−352640.

Date	Date (MJD)	Frequency (GHz)	Array config.
2021-04-05	59309	5.5, 9	6D
2021-06-06	59371	2.1, 5.5, 9	6B
2021-08-21	59447	2.1, 5.5, 9	H214
2021-09-18	59475	2.1	6A
2021-10-05	59492	2.1, 5.5, 9, 16.7, 21.2	6A
2021-11-23	59541	2.1, 5.5, 9, 16.7, 21.2	6C
2022-01-21	59600	2.1, 5.5, 9, 16.7, 21.2	6A
2022-04-04	59673	2.1, 5.5, 9, 16.7, 21.2	6A
2022-08-27	59818	2.1, 5.5, 9, 16.7, 21.2	6D
2022-12-11	59924	2.1, 5.5, 9, 16.7, 21.2	6C
2023-03-17	60 020	2.1, 5.5, 9, 16.7, 21.2	750C
2023-06-07	60 101	2.1, 5.5, 9, 16.7, 21.2	6D

2 OBSERVATIONS

We observed the coordinates of J2344 on 12 occasions with the Australia Telescope Compact Array (ATCA) in the frequency range 2–24 GHz between 2021 April and 2023 June. All observations were taken with the ATCA CABB in the full 2048 spectral channel mode. At each epoch, we observed using some combination of dual receivers with central frequencies of 2.1, 5.5/9, and 16.7/21.2 GHz, which all have 2 GHz of bandwidth. A summary of the observations is given in Table 1.

All ATCA data were reduced using standard procedures in the Common Astronomy Software Application (CASA v 5.6.3; CASA Team et al. 2022), including flux and bandpass calibration with PKS 1934–638 and phase calibration with PKS 2337–334. We imaged the target field using the CASA task `tclean`. For the 16.7/21.2 GHz observations, we used a cellsize of 0.12 and 0.1 arcsec and image size of 2048 pixels, for 5.5/9 GHz, we used a cellsize of 0.3 and 0.2 arcsec and image size of 3000 pixels, and for 2.1 GHz, we used a cellsize of 1 arcsec and image size of 7000 pixels, which resulted in approximately 5 pixels across the synthesized beam for each image. Larger image sizes were required at the lower frequencies in order to deconvolve bright sources in the field of view. Where enough bandwidth was available, we split each frequency band into two sub-bands for imaging, although note that occasionally at 2.1 GHz, severe RFI resulted in much of the band being flagged and only one image was created for the entire frequency band.

In each observation at each frequency, we detected a point source at the location of J2344, which varied in flux density between epochs. We extracted the flux density of the target using the CASA task `imfit`, by fitting an elliptical Gaussian fixed to the size of the synthesized beam. The extracted flux densities and errors are reported in Appendix A. We note that the data collected on 2021-08-21 in H214 configuration were unusable due to the compact array configuration, causing J2344 to be confused with nearby bright sources in the field, so were excluded from the analysis. The 2.1 GHz data collected on 2021-09-18 were combined with the data from 2021-10-05 to increase the sensitivity, resulting in a total of 10 spectral epochs.

2.1 Archival observations

The Rapid ASKAP Continuum Survey (RACS; McConnell et al. 2020; Hale et al. 2021) observed the location of J2344 on 2019 April 29 (0.88 GHz) and 2021 January 10 (1.37 GHz), approximately 2–6 months before and after the X-ray/optical flare. There is no radio source detected in either the RACS-low (0.88 GHz) or RACS-mid (1.37 GHz) observations, with a 3σ upper limit of <0.64 mJy at 0.88 GHz and <0.63 mJy at 1.36 GHz. These radio flux densities provide an upper limit for the host emission as well as the early-time radio emission at 1.37 GHz, and indicate that there is no strong radio AGN activity in the host galaxy. We note that we cannot rule out low-luminosity AGN emission in the host, and indeed the optical spectrum of the galaxy shows strong narrow [O III] emission lines (Homan et al. 2023); a signature of AGN activity.

2.2 Interstellar scintillation

Due to the compact nature of the radio source and its distance, the observed radio flux density is expected to be affected by interstellar scintillation (ISS). To determine the amount of variability expected due to ISS, we use the NE2001 electron density model (Cordes & Lazio 2002) and infer that for the Galactic coordinates of J2344, the transition frequency between strong and weak regimes occurs at 7.75 GHz and the angular size limit of the first Fresnel zone at the transition frequency is 4 μas. Next, using the Walker (1998) formalism as appropriate for extragalactic sources, we find that the radio emission for J2344 will be in the strong refractive scintillation regime until the source reaches an angular size of 70 μas at 2.1 GHz and 8.5 μas at 5.5 GHz. Given the distance of J2344 ($D_A \approx 380$ Mpc), the source will be in the strong scintillation regime until a source size of $\approx 2 \times 10^{17}$ cm at 2.1 GHz and $\approx 2.4 \times 10^{16}$ cm at 5.5 GHz, with variability expected to have a modulation fraction of 0.45–0.01 and occur on time-scales of 35–2 h at 2–21 GHz.

In order to account for the variability induced by ISS between epochs at different frequencies, we introduced an additional uncertainty for each flux density measurement before carrying out the spectral fitting, added in quadrature with the statistical flux density uncertainty. This additional uncertainty varied from 45 per cent at 2 GHz to 30 per cent at 5.5 GHz, and 10 per cent at 9 GHz (in the weak regime). Due to the 16.7 and 21.2 GHz observations being well above the transition frequency in the weak regime, the variability expected due to ISS is of the order of a few per cent and thus is outweighed by the statistical uncertainty. Therefore, we did not include any associated flux density errors at these frequencies. All additional errors due to ISS are listed in Table A1.

3 RESULTS

The radio emission associated with J2344 slowly rose to a peak at 2.1, 5.5, and 9 GHz during the first 300 d of radio observations (corresponding to up to 540 d post-onset of the optical flare). We observed the light curves rise and then decay at all of 9, 5.5, and 2.1 GHz, whereas the radio emission at >16.7 GHz was observed to only decay throughout our monitoring (as shown in Fig. 1). This multifrequency evolution is characteristic of an expanding synchrotron emitting region, where the emission peaks first at higher frequencies and the peak gradually shifts to lower frequencies as the emitting region grows (e.g. Chevalier 1998; Pérez-Torres, Alberdi & Marcaide 2001; Granot & Sari 2002). The time of the radio peak also trails the peak observed at infrared and optical (with the optical occurring first, Fig. 1). This light curve behaviour is similar to other TDEs in which the radio emission was observed to rise slowly hundreds of days after the initial optical flare (e.g. AT2019azh, AT2019dsg AT2020opy; Stein et al. 2021; Cendes et al. 2021b; Goodwin et al. 2022, 2023a).

3.1 Spectral modelling

The broad-band radio spectra of J2344 are well-described by a peaked synchrotron spectrum that evolves over time. In order to constrain the synchrotron properties of the source, we fit each spectrum using the spectral fitting model described in Granot & Sari (2002), similar to the approach used in Alexander et al. (2016); Cendes et al. (2021b); Goodwin et al. (2022, 2023a,b). We assume that the synchrotron emission is in the regime, where the peak is associated with synchrotron self-absorption, i.e. $\nu_m < \nu_a < \nu_c$ (where ν_m is the synchrotron minimum frequency, ν_a is the synchrotron self-absorption frequency, and ν_c is the synchrotron cooling frequency). This is generally the case for non-relativistic outflows in which a blastwave accelerates the ambient electrons into a power-law distribution $N(\gamma) \propto \gamma^{-p}$, where γ is the electron Lorentz factor, p is the synchrotron energy index, and N is the density of electrons (e.g. Barniol Duran, Nakar & Piran 2013). The synchrotron emission is then described by Granot & Sari (2002) as

$$F_{\nu,\mathrm{synch}} = F_{\nu,\mathrm{ext}} \left[\left(\frac{\nu}{\nu_m} \right)^2 \exp\left(-s_1 \left(\frac{\nu}{\nu_m} \right)^{2/3} \right) + \left(\frac{\nu}{\nu_m} \right)^{5/2} \right] \times \left[1 + \left(\frac{\nu}{\nu_a} \right)^{s_2(\beta_1-\beta_2)} \right]^{-1/s_2}, \quad (1)$$

where ν is the frequency, $F_{\nu,\mathrm{ext}}$ is the normalization, $s_1 = 3.63p - 1.60$, $s_2 = 1.25 - 0.18p$, $\beta_1 = \frac{5}{2}$, and $\beta_2 = \frac{1-p}{2}$.

Due to the narrow, high-ionization emission lines of the host galaxy optical spectrum (Homan et al. 2023) and the lack of a strong archival upper limit on the host radio emission, we also include a host component to the observed radio emission, such that the total observed radio emission is described by

$$F_{\nu,\mathrm{total}} = F_{\nu,\mathrm{host}} + F_{\nu,\mathrm{synch}}. \quad (2)$$

In order to constrain $F_{\nu,\mathrm{host}}$ and account for uncertainty in this parameter, we fit all 10 epochs simultaneously, with equation (2), where $F_{\nu,\mathrm{synch}}$ is given by equation (1) and the host emission is described by

$$F_{\nu,\mathrm{host}} = F_0 \left(\frac{\nu}{1.4\,\mathrm{GHz}} \right)^{\alpha_0}, \quad (3)$$

where F_0 is the flux density measured at 1.4 GHz ($F_0 < 0.4$ mJy) and α_0 is the spectral index of the host galaxy.

We use a PYTHON implementation of Markov Chain Monte Carlo (MCMC), `emcee` (Foreman-Mackey et al. 2013) including a Gaussian likelihood function, where the variance is underestimated by some fractional amount f. We allow $F_{\nu,\mathrm{ext}}$, ν_m, and ν_a to be fit individually for each epoch, but only fit a single p, F_0, and α_0 for all epochs. We use flat prior distributions for all parameters. The prior ranges set for each parameter are: $10^{-6} < F_{\nu,\mathrm{ext}} < 10$; $0.5 < \nu_m < \nu_a$; $\nu_m < \nu_a < 10$; $2 < p < 3.5$; $0.001 < F_0 < 0.3$; and $-0.7 < \alpha_0 < -0.3$.

Using this approach, we constrained $F_0 = 0.19 \pm 0.07$, $\alpha_0 = -0.55 \pm 0.13$, and $p = 3.41 \pm 0.06$. We note that $p > 3$ is quite high for synchrotron emission, but is not impossible and is consistent with spectral indices of other TDE radio outflows observed (e.g. Goodwin et al. 2022).

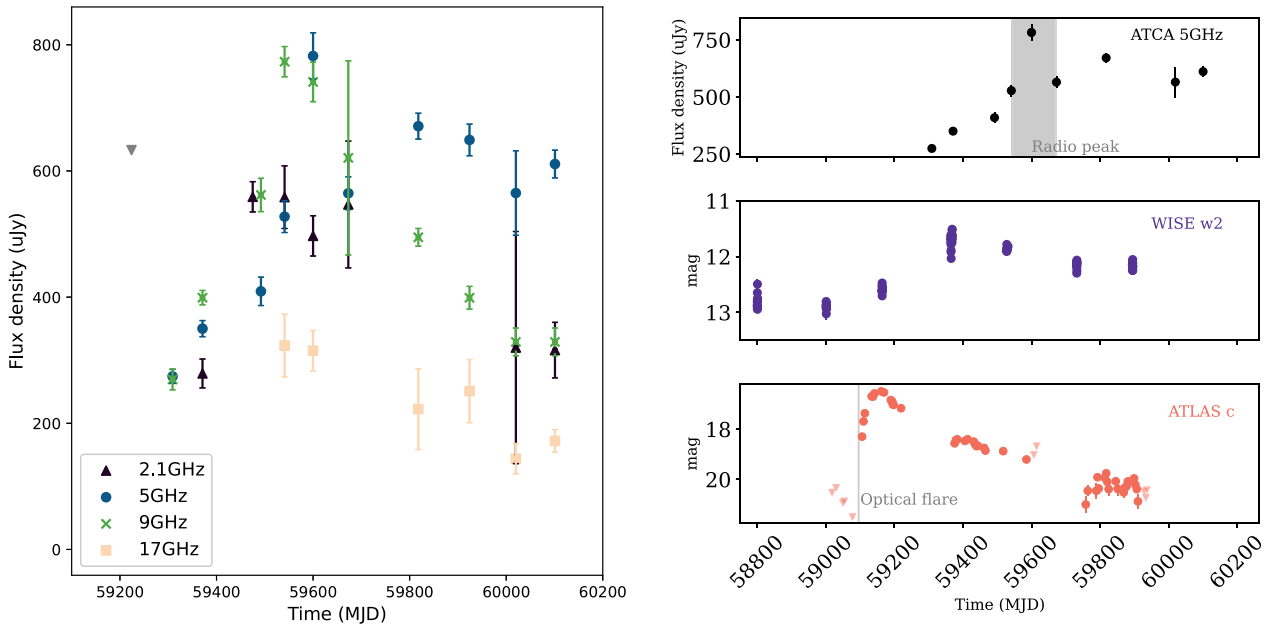

Figure 1. Left: ATCA multifrequency radio light curve of J2344. The radio spectrum peaks first at 9 GHz (green), then 5 GHz (blue) and lastly at 2.1 GHz (purple), characteristic of an expanding synchrotron-emitting region. The grey inverted triangle indicates the 1.37 GHz ASKAP-RACs 3σ upper limit from 2021 January 10. Right: ATCA 5 GHz radio light curve (top), WISE w2 infrared light curve (middle), and ATLAS *c*-band optical light curve (bottom, Homan et al. 2023). The ATLAS data are extracted from difference imaging. The timing of the radio peak and beginning of the optical rise are highlighted in grey-shaded regions, where the width of the region corresponds to the uncertainty in the time. The optical flare clearly leads to the infrared and radio flares, respectively.

The resulting synchrotron spectral fits for each epoch are plotted in Fig. 2, where only the transient emission is shown and the observed data points have had the constrained host component subtracted. The evolution of the peak frequency and peak flux density is plotted in Fig. 3. The peak flux density of the synchrotron spectrum rose for the first 300–400 d before beginning to fade, and the peak frequency in general decreased over the course of the observations, with a large drop between 397–446 d.

3.2 Outflow modelling

Under the assumption that the radio emission observed is described by an expanding synchrotron-emitting region, the physical outflow properties may be estimated under the assumption of equipartition. We use the synchrotron emission equipartition model from Barniol Duran, Nakar & Piran (2013). In order to derive the equipartition radius, R and energy, E, we assume equipartition between the electron and magnetic field energy densities. The exact equations we use to calculate the radius, R, energy, E, ambient electron density, n_e, velocity, β, and magnetic field strength, B are given in Goodwin et al. (2022). The inferred outflow properties are heavily dependent on the assumed geometry of the outflow, where the geometry is described by geometric factors given by $f_A = A/(\pi R^2/\Gamma^2)$ and $f_V = V/(\pi R^3/\Gamma^4)$, for area, A, and volume, V, of the outflow, and distance from the origin of the outflow, R (Barniol Duran, Nakar & Piran 2013). Since the outflow geometry is not known, we include two geometries in our analysis: a 'spherical' geometry where $f_A = 1$ and $f_V = 4/3$; and a 'conical' geometry appropriate for a mildly collimated jet where $f_A = 0.13$ and $f_V = 1.15$.

Assuming equipartition allows us to estimate the key physical quantities; however, the emitting region is likely not in equipartition. We therefore apply a post-correction to the physical quantities to correct for any expected deviation from equipartition. For this correction, we assume that the fraction of the total energy of the outflow in the magnetic field is 2 per cent, i.e. $\epsilon_B = 0.02$ based on observations of TDEs and supernovae (Horesh et al. 2013; Cendes et al. 2021a). We additionally assume that 10 per cent of the total energy is carried by the electrons, i.e. $\epsilon_e = 0.1$ as has been adopted in other TDE outflow analyses (e.g. Alexander et al. 2016; Cendes et al. 2021a; Goodwin et al. 2022). However, we note that recent studies have found $\epsilon_e \sim 10^{-3}$–10^{-4} for non-relativistic collisionless shocks (Park, Caprioli & Spitkovsky 2015; Xu, Spitkovsky & Caprioli 2020). For reference, in Appendix B, we include the outflow properties calculated for different assumed ϵ_e and note that smaller ϵ_e results in slightly larger radii and energies and a lower inferred ambient electron density.

The calculated properties of the outflow are listed in Table 2 and plotted in Fig. 4.

4 CONSTRAINTS ON THE OUTFLOW LAUNCHED

The radius constraints obtained via the equipartition modelling enable a launch date of the outflow to be estimated. A simple linear fit to the radii assuming constant velocity of the outflow results in an outflow launch date of MJD 58784 ± 3 d (spherical) or MJD 58953 ± 3 d (conical), earlier than the estimated onset of the optical flare date (MJD 59095 ± 1, Homan et al. 2023). The reduced-χ^2 statistic for these two fits are 5.39 and 6.7, respectively, indicating the data are poorly fit by a single linear model. We instead fit the first five epochs with a linear model, before the onset of deceleration of the outflow. In these cases, we constrain an outflow launch date of MJD 59054 ± 1 d (spherical) or MJD 59041 ± 3 d (conical), just 5–18 d earlier than the estimated onset of the optical flare date.

Alternatively, assuming the outflow velocity is not constant and the outflow is decelerating with time, we also fit a power law to the

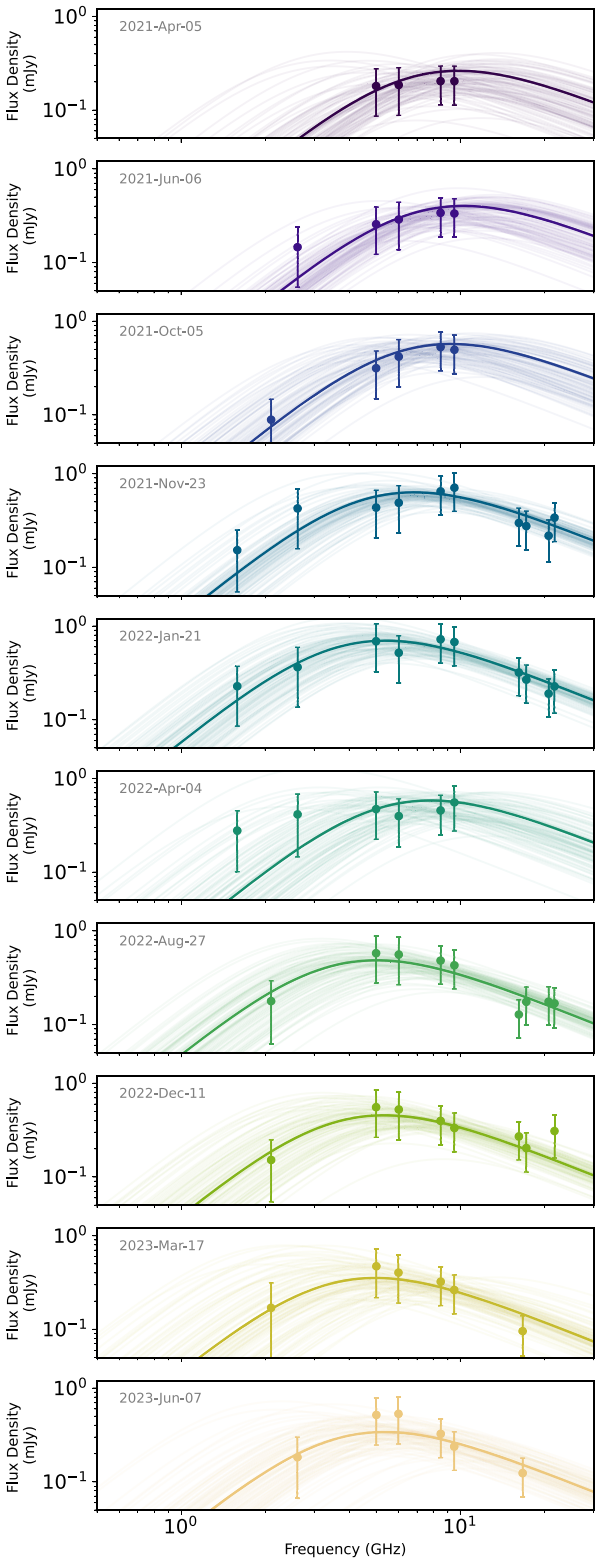

Figure 2. Spectral fits of the transient component of the radio emission assuming synchrotron emission, where the peak is associated with the self-absorption break for each of the 10 epochs of ATCA observations of J2344. Solid dark lines indicate the best-fit spectrum, while lighter lines indicate 100 random samples from the MCMC distribution of spectral fits to demonstrate the approximate uncertainty in the fits. It is apparent that the peak of the spectrum shifts to a lower frequency over time.

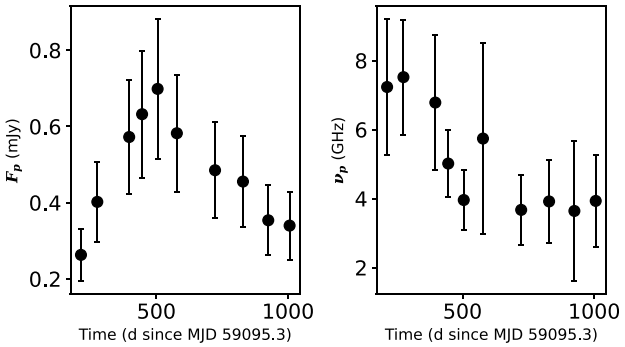

Figure 3. Left: Peak flux density evolution with time for the synchrotron spectral fits of each epoch. Right: Peak frequency evolution with time for the synchrotron spectral fits of each epoch. The peak flux density of the synchrotron spectrum rose for the first 300–400 d before beginning to fade, and the peak frequency in general decreased over the course of the observations, although there was a sharp drop between 397–446 d.

predicted radius evolution with time, where the radius evolution with time is described by:

$$R = A(t - t_0)^{\alpha}, \tag{4}$$

where t_0 is the outflow launch time. Using this equation, we constrain $\alpha = 0.47^{+0.07}_{-0.08}$, $t_0 = 59164 \pm 60$ MJD (spherical), or $\alpha = 0.59^{+0.06}_{-0.06}$, $t_0 = 59141 \pm 55$ MJD (conical). The reduced-χ^2 statistic for these two fits are 4.17 and 4.49, respectively, indicating a better fit than the simple linear model above. In the case of a decelerating outflow, the outflow launch date is therefore approximately 27–165 d after the observed onset of the optical flare.

While the case of a decelerating outflow predicts an outflow launch date t_0 approximately consistent with or up to 165 d after the onset of the optical rise date (Fig. 4 lower-left-hand panel), a linear fit to the radius assuming constant velocity for the entire span of the observations predicts an outflow launched up to 200 d prior to the optical flare, or only for the first five epochs predicts an outflow launched up to 20 d prior to the optical flare. This modelling indicates that a decelerating model is supported if the outflow was launched around the time of the optical flare.

4.1 Single ejection outflow

The increasing energy during the first ≈500 d post-optical flare of the outflow could be either due to an off-axis relativistic jet decelerating and widening into view (which we explore in Section 4.2.1), or a freely coasting shock front launched at the time of the optical/X-ray/UV flare. In this latter scenario, a single ejection of material creates a shock front that interacts with the surrounding material, the CNM, similar to the forward shock in a supernova (Chevalier 1982a,b; Weiler et al. 1986; Chevalier 1998; Weiler et al. 2002). The geometry of this ejecta depends on the mechanism that produced it, where our spherical model in Table 2 corresponds to an outflow launched by a TDE from stream–stream collisions or disc winds, and our conical model in Table 2 corresponds to a collimated outflow launched either by a TDE accretion episode or sudden accretion epsiode in a pre-existing AGN. Regardless of the ejecta geometry, during the expansion, the shock front interacts with and heats the CNM material, sweeping up mass and transferring energy to the shocked region. This scenario has also been suggested to explain the increasing energy observed for the TDE AT2019dsg (Matsumoto, Piran & Krolik 2022). The electron cooling time-scale is much longer

Table 2. Equipartition modelling properties of the outflow produced by J2344 based on the synchrotron spectral fits. We report both the uncorrected equipartition radius (R_{eq}) and energy (E_{eq}) as well as the corrected radius (R) and energy (E). The time for each epoch is measured with respect to the optical flare date, MJD 59059.

	Time (d)	F_p (mJy)	ν_p (GHz)	log R_{eq} (cm)	log E_{eq} (erg)	log R (cm)	log E (erg)	β	log B (G)	log n_e (cm^{-3})	log M_{ej} (g)
	214	0.26 ± 0.07	7.23 ± 1.96	16.42 ± 0.13	49.06 ± 0.18	16.39 ± 0.13	49.10 ± 0.18	0.05 ± 0.01	−0.03 ± 1.75	4.04 ± 1.23	31.12 ± 0.22
	276	0.40 ± 0.10	7.52 ± 1.66	16.49 ± 0.11	49.27 ± 0.17	16.46 ± 0.11	49.31 ± 0.17	0.04 ± 0.01	−0.03 ± 1.47	4.03 ± 1.05	31.40 ± 0.20
	397	0.57 ± 0.15	6.78 ± 1.96	16.60 ± 0.14	49.50 ± 0.19	16.58 ± 0.14	49.54 ± 0.19	0.04 ± 0.01	−0.09 ± 1.60	3.91 ± 1.30	31.71 ± 0.23
	446	0.63 ± 0.17	5.02 ± 0.97	16.75 ± 0.10	49.68 ± 0.16	16.73 ± 0.10	49.73 ± 0.16	0.05 ± 0.01	−0.23 ± 0.84	3.64 ± 0.96	31.70 ± 0.19
Spherical	505	0.70 ± 0.18	3.96 ± 0.86	16.88 ± 0.11	49.84 ± 0.17	16.85 ± 0.11	49.88 ± 0.17	0.06 ± 0.01	−0.34 ± 0.72	3.43 ± 1.04	31.73 ± 0.20
	578	0.58 ± 0.15	5.74 ± 2.76	16.68 ± 0.22	49.58 ± 0.25	16.65 ± 0.22	49.62 ± 0.25	0.03 ± 0.02	−0.17 ± 2.15	3.77 ± 2.03	31.96 ± 0.33
	723	0.49 ± 0.13	3.67 ± 1.00	16.84 ± 0.13	49.68 ± 0.18	16.81 ± 0.13	49.72 ± 0.18	0.04 ± 0.01	−0.35 ± 0.84	3.40 ± 1.24	31.94 ± 0.22
	829	0.46 ± 0.12	3.92 ± 1.21	16.79 ± 0.14	49.62 ± 0.19	16.77 ± 0.14	49.66 ± 0.19	0.03 ± 0.01	−0.32 ± 1.00	3.46 ± 1.37	32.08 ± 0.24
	925	0.35 ± 0.09	3.64 ± 2.03	16.77 ± 0.25	49.51 ± 0.28	16.75 ± 0.25	49.56 ± 0.28	0.03 ± 0.01	−0.34 ± 1.65	3.42 ± 2.33	32.11 ± 0.37
	1006	0.34 ± 0.09	3.93 ± 1.32	16.73 ± 0.16	49.46 ± 0.20	16.71 ± 0.16	49.50 ± 0.20	0.02 ± 0.01	−0.31 ± 1.12	3.49 ± 1.48	32.20 ± 0.25
	214	0.26 ± 0.07	7.23 ± 1.96	16.79 ± 0.13	49.62 ± 0.18	16.77 ± 0.13	49.67 ± 0.18	0.09 ± 0.03	−0.29 ± 0.97	3.53 ± 1.23	31.10 ± 0.22
	276	0.40 ± 0.10	7.52 ± 1.66	16.87 ± 0.11	49.83 ± 0.17	16.84 ± 0.11	49.87 ± 0.17	0.09 ± 0.02	−0.29 ± 0.82	3.52 ± 1.05	31.35 ± 0.20
	397	0.57 ± 0.15	6.78 ± 1.96	16.98 ± 0.14	50.06 ± 0.19	16.96 ± 0.14	50.11 ± 0.19	0.08 ± 0.03	−0.35 ± 0.89	3.40 ± 1.30	31.63 ± 0.23
	446	0.63 ± 0.17	5.02 ± 0.97	17.13 ± 0.10	50.25 ± 0.16	17.11 ± 0.10	50.29 ± 0.16	0.10 ± 0.02	−0.48 ± 0.47	3.13 ± 0.96	31.62 ± 0.19
Conical	505	0.70 ± 0.18	3.96 ± 0.86	17.26 ± 0.11	50.40 ± 0.17	17.23 ± 0.11	50.45 ± 0.17	0.12 ± 0.03	−0.59 ± 0.40	2.92 ± 1.04	31.65 ± 0.20
	578	0.58 ± 0.15	5.74 ± 2.76	17.06 ± 0.22	50.14 ± 0.25	17.03 ± 0.22	50.19 ± 0.25	0.07 ± 0.03	−0.42 ± 1.20	3.26 ± 2.03	31.85 ± 0.33
	723	0.49 ± 0.13	3.67 ± 1.00	17.21 ± 0.13	50.24 ± 0.18	17.19 ± 0.13	50.28 ± 0.18	0.08 ± 0.02	−0.61 ± 0.47	2.89 ± 1.24	31.83 ± 0.22
	829	0.46 ± 0.12	3.92 ± 1.21	17.17 ± 0.14	50.18 ± 0.19	17.15 ± 0.14	50.22 ± 0.19	0.06 ± 0.02	−0.58 ± 0.56	2.95 ± 1.37	31.95 ± 0.24
	925	0.35 ± 0.09	3.64 ± 2.03	17.15 ± 0.25	50.08 ± 0.28	17.13 ± 0.25	50.12 ± 0.28	0.06 ± 0.03	−0.60 ± 0.92	2.91 ± 2.33	31.97 ± 0.37
	1006	0.34 ± 0.09	3.93 ± 1.32	17.11 ± 0.16	50.02 ± 0.20	17.09 ± 0.16	50.07 ± 0.20	0.05 ± 0.02	−0.56 ± 0.62	2.98 ± 1.48	32.06 ± 0.25

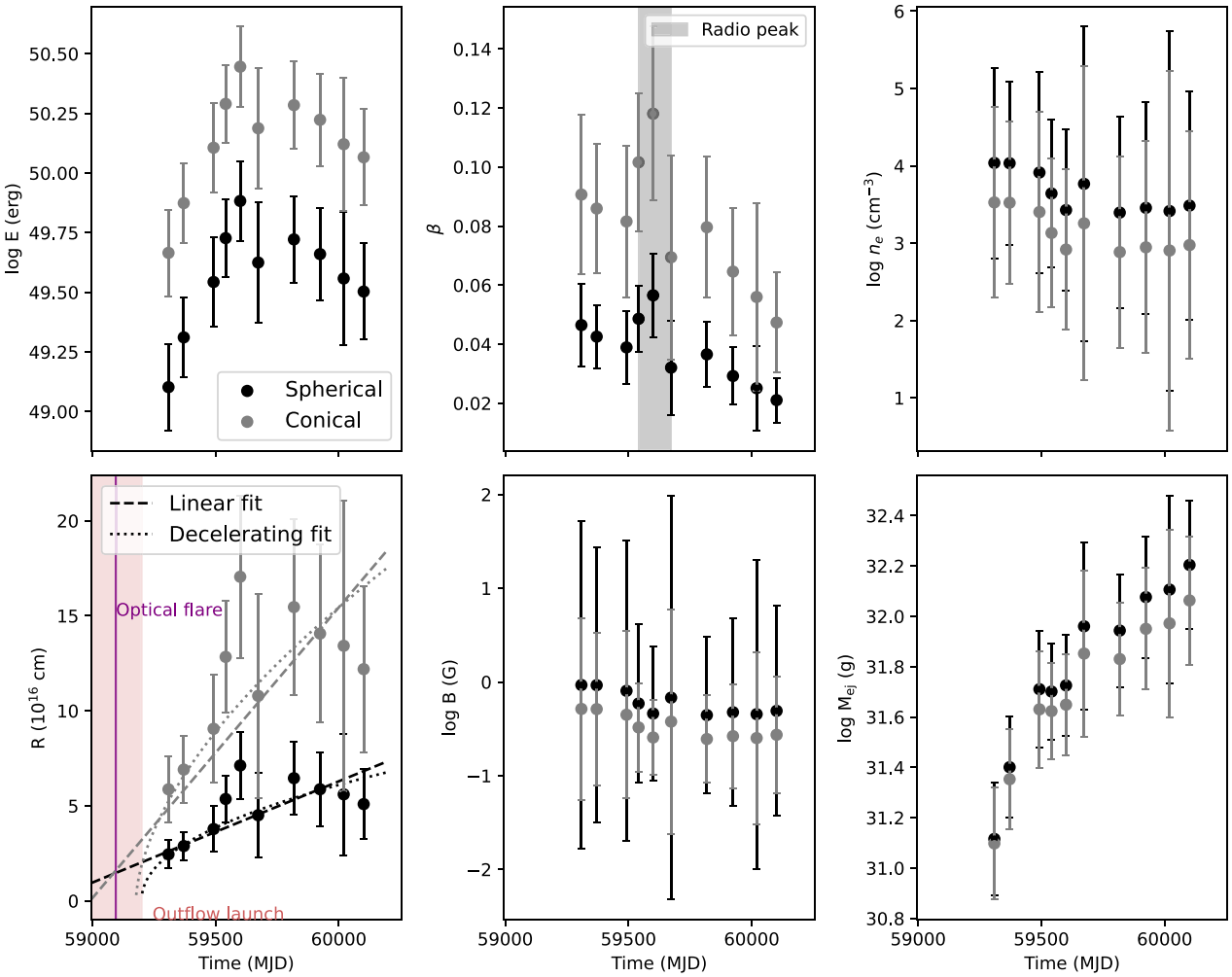

Figure 4. Physical outflow properties inferred from equipartition modelling of the spectral properties of the radio emission from J2344. Properties derived with an assumed spherical geometry are plotted in black, and ones with a conical geometry in grey. E and R are the estimated energy and radius of the outflow derived from an equipartition analysis and corrected for assumed deviation from equipartition. β is the outflow velocity divided by the speed of light, B is the magnetic field strength, n_e is the free electron number density of the ambient medium, and M_{ej} is the mass in the ejecta. The dashed lines in the lower left-hand panel show a linear fit to the radius for each geometry and the dotted lines show a power-law fit to the radius for each geometry, assuming a decelerating outflow. The onset of the optical rise time is indicated in purple shading, and the estimated outflow launch date (when $R = 0$) is indicated in red shading.

than the dynamical time, where the cooling time-scale is related to the magnetic field via

$$t_{\rm cool} = 4500\,{\rm d}\left(\frac{\rm B}{1{\rm G}}\right)^{-2}\left(\frac{\gamma_{\rm m}}{2}\right)^{-1}. \quad (5)$$

Therefore, negligible energy is lost to cooling of the electron population over the course of our observations.

Matsumoto, Piran & Krolik (2022) showed that for a freely expanding outflow that is increasing in energy by sweeping up material from the CNM, the expected evolution of kinetic energy with time is dependent on the gradient of the density of the CNM, k, such that

$$E \propto t^{(5-k)\alpha-2}, \quad (6)$$

where α is the power-law index, $R \propto (\Delta t - t_0)^{\alpha}$. In Section 4.1.1, we constrain for a decelerating outflow $\alpha = 0.47^{+0.07}_{-0.08}$ (spherical), $\alpha = 0.59^{+0.06}_{-0.06}$ (conical), or $\alpha = 1$, assuming constant velocity and therefore linear radial growth with time.

Fitting a power law to the kinetic energy over all observations of J2344 in Fig. 4, $E \propto (t - t_0)^{\beta}$, we find $\beta = 0.46^{+0.18}_{-0.11}$ (decelerating) or $0.41^{+0.06}_{-0.04}$ (constant velocity) for the spherical case, and $\beta = 0.62^{+0.17}_{-0.09}$ (decelerating) or $0.62^{+0.09}_{-0.06}$ (constant velocity) for the conical case. We therefore find $k = 0.2$–1 (decelerating, spherical/conical) or 2.3–2.6 (constant velocity, spherical/conical).

Additionally, a power law fit to the predicted radius and ambient density in Fig. 4 gives $n \propto r^{-1.4}$, i.e. $k = 1.4$, consistent with the CNM density gradients we infer from the energy modelling above. Although we note the large error bars on the ambient density estimates mean this fit is not particularly well constrained. Therefore, the initially increasing energy/flux density of the radio flare is well explained by a single injection of material into an initially ballistically expanding outflow, shocking the CNM, sweeping up material, and producing additional energy that began decelerating after the peak radio brightness. Similar increasing energies have been observed in synchrotron-emitting outflows from supernovae and attributed to CNM interactions (Salas et al. 2013; Anderson et al. 2017) and in TDEs such as AT2019dsg (Stein

et al. 2021; Cendes et al. 2021b) and AT2019azh (Goodwin et al. 2022).

4.1.1 *Deceleration time and peak radio flux density*

The peak radio flux density for J2344 initially rose, until MJD 59600 ± 65 d (505 d post-optical flare), at which time the peak flux density began to fall (Fig. 3). When the outflow sweeps up mass approximately equal to the initial mass in the outflow, it will begin to decelerate and no longer produce additional energy. The decay of the radio emission and transition to constant kinetic energy can be explained by the deceleration of the outflow. In the deceleration phase, the light curve is expected to evolve following a Sedov–Taylor decay. In the case of a freely expanding outflow, theoretically, the time of peak radio flux density should correspond to the deceleration time, or the time at which the outflow has swept up equivalent mass from the CNM to the original mass in the ejecta (Lu & Bonnerot 2020a). After this time, the outflow will enter the Sedov–Taylor decay phase if no additional energy is deposited. The deceleration radius for a freely expanding shock front is given by Lu & Bonnerot (2020a)

$$r_{\rm dec,pc}^{3-k} = \frac{3-k}{\Omega}\frac{2E_k}{N_{\rm pc}m_{\rm p}v_0^2}, \tag{7}$$

where $N_{\rm pc} = n_{\rm pc}(1{\rm pc})^3$ is a reference number of electrons, $m_{\rm p}$ is the proton mass, v_0 is the initial velocity, E_k is the kinetic energy of the outflow, Ω is the solid angle the outflow covers (for a spherical outflow we assume $\Omega = 2\pi$), and k is related to the ambient density profile via $n = n_{\rm pc}r_{\rm pc}^{-k}$ ($k < 3$).

For J2344, the outflow modelling in Section 3.2 produces significantly different outflow energies, velocities, radii, and ambient densities depending on assumptions about the geometry and equipartition. Therefore, taking the widest range in the outflow parameters (for changing geometry and equipartition), we find for a kinetic energy of $E_k \sim 1 \times 10^{49}$ to 1×10^{53} erg, velocity ∼0.05 to ∼0.3c, and ambient density $n_{\rm e} \sim 10^3$ to 10^{-1} cm^{-3}, and assuming $k = 2$ and $\Omega = 2\pi$, we find the deceleration radius could be anywhere from 8×10^{14} to 2×10^{21} cm and the onset of deceleration time could be anywhere from 6 d to 8000 yr post outflow launch. If we take the peak radio flux density of the light curve to correspond to the deceleration time, this occurred between 397–505 d post-outflow launch at a predicted radius of 5.3×10^{16} (spherical) or 1.3×10^{17} cm (conical). While the predicted deceleration time is subject to many assumptions and is therefore quite uncertain, the observed time of the radio peak is within the expected time range at which the outflow should have begun decelerating if the radio emission observed is described by an initially ballistic outflow model. Additionally, the deceleration time measured would imply the equipartition parameters are closer to those presented in Table 2 than those in Table B1, i.e. the fraction of total energy of the outflow carried by the electrons is closer to 10 than 0.01 per cent or lower.

In this deceleration phase, the flux density evolution of the fading shockwave is proportional to the CNM density gradient and synchrotron spectral indices (Sironi & Giannios 2013) and can be described by a spherical shock-front impacting a stratified medium with density profile $n \propto r^{-k}$ and the electrons in the shock are accelerated into a power-law distribution ${\rm d}N_{\rm e}/{\rm d}\gamma \propto \gamma^{-p}$, where γ is the electron Lorentz factor. The radio luminosity is thus related to time via

$$L_\nu = \nu^{(1-p)/2}t^{-(2(3-k)(p-3)+3(p+1)/(2(5-k)))}. \tag{8}$$

In Fig. 5, we plot the 5 GHz luminosity evolution of J2344 as well as two predicted Sedov–Taylor luminosity decays for $k = 1$ and 2, fixing $p = 2.7$. Evidently, the flatter $k = 1$ CNM density gradient is preferred for the evolution of the luminosity decay of J2344. We therefore find that both the early pre-radio peak evolution and late post-radio peak evolution of the outflow emission can be explained by a single ejection of material from near the central SMBH, and a ballistic outflow impacting a CNM with a relatively flat density profile such that $n \propto r^{-1}$.

4.2 Jet-like outflow

Alternatively, the observed radio flare may be a signature of a jet that was launched coincident with the optical flare, or shocks in a pre-existing jet of an AGN (i.e. our conical model in Table 2), although the archival non-detections of the host galaxy in the ASKAP-RACS radio survey rule out a bright pre-existing AGN jet in the system. In this scenario, the increasing energy may be due to continuous energy injection into the outflow from the accreting SMBH. The rate of increase in energy enables a constraint on the required luminosity injection rate, i.e.

$$L_{\rm in} \sim \frac{{\rm d}E_{\rm eq}}{{\rm d}t} \approx 3.36 \times 10^{43}\left(\frac{t}{64\,{\rm d}}\right)^{0.95}\,{\rm erg\,s^{-1}}, \tag{9}$$

where 64 d is the time from optical flare to peak optical brightness (Homan et al. 2023) and we have assumed $E_{\rm eq} = At^B$, constraining $A = (3.07 \pm 5) \times 10^{44}$ and $B = 1.95 \pm 0.3$ by fitting the constrained energies during the period the energy was increasing (Fig. 4).

In comparison, the fallback luminosity of a solar mass star disrupted by a 10^7 M$_\odot$ black hole is

$$L_{\rm fb} \sim \dot{M}c^2 \sim 10^{47}\left(\frac{t}{111\,{\rm d}}\right)^{-5/3} R_* M_*^{1/3} M_{\rm SMBH,7}^{-2/3}\,{\rm erg\,s^{-1}}, \tag{10}$$

where R_* and M_* are the radius and mass of the disrupted star, respectively, in solar mass and radii units, $M_{\rm SMBH,\,7}$ is the mass of the black hole in 10^7 M$_\odot$.

The fallback luminosity is approximately four orders of magnitude larger than the luminosity required by the energy injection rate if the increasing energy were powered by injection into the outflow from the accreting SMBH. In order for the increasing energy of the outflow to be explained by continuous energy injection from accretion, the efficiency of accretion would have to be extremely high, with only 0.03 per cent of the accreted material being injected into the outflow.

Additionally, the X-ray emission observed from this event also enables an estimate of the accretion rate. The observed X-ray luminosity is $L_{0.2\text{–}2\,{\rm keV}} = 7.94 \times 10^{44}$ erg s^{-1} (Homan et al. 2023). Assuming approximately 10 per cent of the accreted mass is converted into the 0.2–2 keV luminosity (e.g. Auchettl, Ramirez-Ruiz & Guillochon 2018), this implies an accretion luminosity of $L_{\rm acc} \sim 8 \times 10^{45}$ erg s^{-1}, meaning that just 0.8 per cent of the accreted material is required to be injected into the outflow to power the increasing energy observed, again requiring extremely efficient accretion.

4.2.1 *Off-axis relativistic jet-like outflow*

Recently, Matsumoto & Piran (2023) extended the equipartition method to relativistic off-axis emitters. Here, we assess whether the radio emission from J2344 is well described by an off-axis relativistic jet-like outflow. In the case of an off-axis relativistic jet, the initially relativistic jet eventually decelerates and becomes Newtonian, at which time the two branches of the equipartition

solutions merge and a single solution for the outflow is obtained. In the case of an initially relativistic, off-axis jet, at this transition time the equipartition Newtonian velocity must be $\beta_{\rm Eq,\,N} > 0.23$, where (Matsumoto & Piran 2023) define

$$\beta_{\rm Eq,N} \approx 0.73 \left[\frac{(F_{\rm p}/{\rm mJy})^{8/17} (d_{\rm L}/10^{28}\,{\rm cm})^{16/17} \eta^{35/51}}{(\nu_{\rm p}/10\,{\rm GHz})(1+z)^{8/17}} \left(\frac{t}{100\,{\rm d}} \right)^{-1} \right] \times f_{\rm A}^{-7/17} f_{\rm V}^{-1/17}, \quad (11)$$

where all parameters are as defined in Section 3.2.

For J2344, $\beta_{\rm Eq,\,N}$ only exceeds 0.23 for jet geometries with a half-opening angle $<15°$, and only for the highest velocity epochs at 440–550 d post optical flare. For the two geometries considered throughout this work, $\beta_{\rm Eq,\,N}$ never exceeds 0.23, and has been decreasing since the peak at ≈500 d.

The observations we present of J2344 indicate that both the peak flux density and peak frequency have been declining for the past 500 d. The peak flux density is declining as $F_{\rm p} \propto t^{-1.05}$ and the peak frequency has been declining as $\nu_{\rm p} \propto t^{-0.35}$ (Fig. 3). Therefore, the equipartition Newtonian velocity (equation (11)) is proportional to $\beta_{\rm Eq,\,N} \propto t^{-1.14}$. Similarly to the case of AT2019dsg discussed by Matsumoto & Piran (2023), unless these trends change and either $F_{\rm p}$ begins to increase or $\nu_{\rm p}$ begins to decrease more rapidly for J2344, the transition from the Newtonian branch to the relativistic branch of the equipartition solutions will never happen. In this scenario, the outflow cannot be described by an off-axis relativistic jet launched by a tidal disruption event.

5 DISCUSSION

Our broad-band multi-epoch radio spectral observations reveal a radio flare associated with the nuclear transient J2344. The radio flare rose to a peak luminosity of $\sim 10^{39}$ erg s^{-1} over ∼500 d post-optical flare start and showed spectral evolution characteristic of an expanding synchrotron-emitting region due to an outflow. Through modelling of the synchrotron emission and outflow properties using an equipartition approach, we infer that the outflow was launched approximately coincident with the onset of the optical flare (within 100 d). The question remains: what kind of nuclear transient event can explain the multiwavelength properties that were observed?

Homan et al. (2023) analysed the initial optical, X-ray, UV, and infrared flare that was observed from J2344. They deduced that the soft X-ray spectrum, rapid onset of decay in X-ray, UV, and optical, and optical spectrum are indicative of a TDE. However, they note that the high-ionisation narrow lines present in the optical spectrum are indicative that the galaxy is likely a low-luminosity AGN or was in a more active AGN phase as recently as a few millennia ago. Below, we discuss the likely nature of the transient event in the context of the radio flare that we discovered.

We modelled the synchrotron emission using an equipartition approach and found the radius increased over the 1000 d of radio observations, while the ambient density decreased, the mass in the emitting region increased, and the magnetic field strength remained approximately constant. The radio emission is consistent with an outflow with radii from 10^{16}–10^{17} cm, energy 10^{49}–10^{50} erg, and velocity 5–10 per cent c. Interestingly, the total kinetic energy of the outflow increased steadily until ∼500 d post-outflow launch, at which time, the energy plateaued. The plateau in energy corresponds to the peak radio luminosity of the light curve. At the same time, the velocity also remained approximately constant during the energy plateau phase, following which it declined.

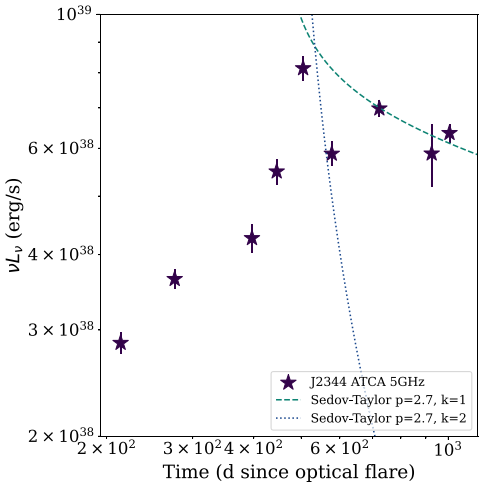

Figure 5. Radio luminosity of J2344 and the predicted flux density evolution during the Sedov–Taylor decay phase for two different CNM density distributions, $n \propto r^{-k}$, assuming an electron energy index $p = 2.7$.

5.1 TDE interpretation

TDEs are known to launch outflows that are observed as transient radio emission evolving on time-scales of ∼months (e.g. Alexander et al. 2020). The mechanism that launches non-relativistic outflows is currently under debate, with leading theories involving either a mildly collimated jet (e.g. Stein et al. 2021; Cendes et al. 2022), disc-wind (e.g. Alexander et al. 2016), debris stream collisions (Lu & Bonnerot 2020b), or the unbound debris stream (Krolik et al. 2016). Recent studies have unveiled a population of prompt-radio emitting TDEs in which the outflow radius can be tracked back to launch dates coincident with the optical flare (e.g. Cendes et al. 2021b; Goodwin et al. 2022, 2023a,b), suggesting prompt launching of the outflow from either debris stream collisions or the unbound debris stream. Most models predict the debris circularization would occur on longer time-scales and thus delay the production of an outflow launched via accretion processes (i.e. jet or disc winds). These types of outflows appear to also be possible, with a new population of radio-emitting TDEs recently discovered that appear to have launched outflows 100 to 1000s of days after the initial optical flare (Cendes et al. 2023), in contrast to the prompt radio-emitters.

The inferred outflow launch date for J2344, approximately coincident with the initial optical flare, would imply an outflow launched by either debris stream collisions or the unbound debris stream. The outflow properties in this model (stream collisions spherical, unbound debris conical, Table 2) are very consistent with both of those scenarios (velocity ∼0.05–0.10c, energy $\sim 10^{49}$ erg; Krolik et al. 2016; Lu & Bonnerot 2020a). Since the outflow was likely launched around the time of the initial optical flare, in this scenario, it is therefore related to the optical flare that was observed from the nucleus of this galaxy. The radio observations of J2344 further enhance the case of the transient being triggered by a TDE within a low-luminosity AGN (LLAGN).

5.1.1 Comparison to other TDEs

The radio properties of J2344 are consistent with those of other radio-detected TDEs that launched non-relativistic outflows (Figs 6 and 7). The peak radio and optical luminosities of J2344 are among the brightest of the population of events, perhaps indicating a correlation

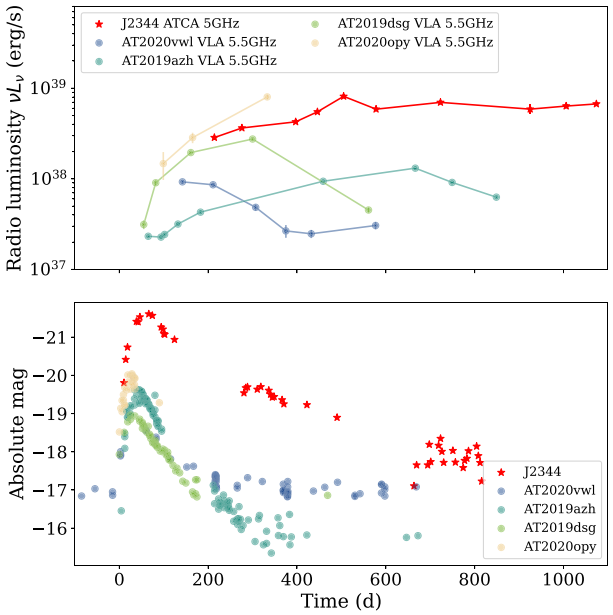

Figure 6. Top: Radio luminosity of J2344 (red stars) and a selection of other radio-detected TDEs with good light curve coverage. Bottom: Optical ATLAS *c*-band light curve of J2344 (Homan et al. 2023) and *Gaia g*-band light curves of the same selection of TDEs, converted to absolute magnitude. The ATLAS data are extracted from different imaging. All *Gaia* light curves were obtained from the *Gaia* photometric science alerts data base (http://gsaweb.ast.cam.ac.uk/alerts; Gaia Collaboration et al. 2016)). Times on the *x*-axis have been scaled to the approximate onset of the optical rise for each event. The flatter radio decay of J2344 may be due to a flatter density distribution in the central regions of the host galaxy.

between the optical overluminosity of this event and the luminosity of the radio emission in which more violent stream–stream collisions could result in a larger CIO. Further radio observations of optical overluminous TDEs would enable confirmation of this trend.

While J2344 appears to have a much flatter luminosity decay than other long-lived radio TDEs, such as AT2019azh (Fig. 6), this can be explained by a slightly flatter CNM density distribution in the host galaxy, as indicated by the outflow energetics described in Section 4.2. Additionally, recent late-time radio observations of TDEs are revealing that late-time rising radio emission is relatively common in TDEs, regardless of whether early-time radio emission was detected or not (Cendes et al. 2023). Therefore, a flattening or even re-brightening of the radio light curve of J2344 would not be unexpected for a TDE origin, where renewed brightening might be due to a second outflow launched by a different process. Both the time-scales of the radio rise and decay with respect to the optical flare are broadly consistent with the TDE population. The predicted energy and velocity of the outflow that was launched also fit well with those predicted for other non-relativistic TDEs (Fig. 7).

We note that the TDE ASASSN-14li is a well-known TDE to have occurred in an LLAGN (Alexander et al. 2016), so the presence of AGN-like emission lines in the optical spectrum of J2344 (Homan et al. 2023) does not preclude the possibility of a TDE occurring in the galaxy.

5.2 AGN flare interpretation

Given the narrow emission lines in the optical spectrum of the host galaxy of J2344 (Homan et al. 2023), an AGN flare is a natural interpretation for the variability that was observed in the nucleus of the galaxy. AGN often show variability across the electromagnetic spectrum, including the radio (e.g. Valtaoja et al. 1992b). Radio variability of AGN is most often attributed to shocks in the jets that are the source of the radio emission, as opposed to a single ejection of material that then expands (e.g. Marscher & Gear 1985; Valtaoja et al. 1992a). Broad blue-shifted absorption lines in some AGN X-ray and/or UV spectra are attributed to AGN disc winds (e.g. Fabian 2012), which can be the cause of some AGN variability. The fastest of these winds, at 0.1–0.3 c contain highly ionized gas detectable only at X-ray energies (Fiore et al. 2017), however, given the lack of X-ray absorption lines in the X-ray observations J2344, we find the observed radio flare unlikely to be driven by an AGN disc-wind. In AGN adiabatic shock-in-jet flare models, an adiabatic shock develops near the base of the jet, and moves downstream, producing radio emission from synchrotron radiation that peaks at lower frequencies over time (Valtaoja et al. 1992a). This model requires a pre-existing jet in the system.

Below we analyse the radio variability properties of J2344 and compare to other radio flares observed from AGN. Hovatta et al. (2008) analysed the long-term radio variability of 55 AGN between 4.8 and 230 GHz. They observed 159 individual AGN flares and extracted the characteristics of these flares. On average, at 4.8 GHz, they found that the median duration of a flare was 2.9 yr and the median variability index was 0.53, where they define the variability index as

$$V = \frac{(S_{\max} - \sigma_{S_{\max}}) - (S_{\min} + \sigma_{S_{\min}})}{(S_{\max} - \sigma_{S_{\max}}) + (S_{\min} + \sigma_{S_{\min}})}, \tag{12}$$

where $S_{\max}$ is the maximum observed flux density with error $\sigma_{S_{\max}}$ and $S_{\min}$ is the minimum flux density with error $\sigma_{S_{\min}}$.

Using equation (12), we calculate that at 5 GHz for J2344 $V >$ 0.478 and a lower limit on the flare duration to be $>$2.3 yr. This level of variability is consistent with the variability seen in AGN flares, although the true baseline flux of J2344 is not known so the true variability index may be higher.

However, AGN that exhibit flares usually flare multiple times (e.g. Pyatunina et al. 2007). Repeated flaring would be a clear sign of AGN activity rather than a TDE (Auchettl, Ramirez-Ruiz & Guillochon 2018). Long-term optical and infrared *Gaia* and WISE monitoring of J2344 dating back to 2014 show no previous flaring activity (Homan et al. 2023) and the available archival radio observations of J2344 show no sign of previous radio activity. Future longer time baseline monitoring of the galaxy to search for additional flares may help constrain the AGN-flare model.

In Section 4, we analysed the modelled outflow properties of J2344 in the case that the radio flare was a signature of a jet either launched coincident with the optical flare or shocks in a pre-existing jet of an AGN. We find it unlikely that the radio emission is explained by shocks in a pre-existing jet, as the optical flare would be unlikely to lead the radio flare in that case as was observed, as the optical and radio emission would be produced by the same mechanism (e.g. Valtaoja et al. 1992a). Additionally, we disfavour a jet from a TDE explanation for the radio outflow due to the extremely high efficiency of accretion that would be required to explain the energy observed in the outflow of this event. In the case of an AGN, the accretion rate may be lower, and therefore the efficiency of accretion need not be so high in order to explain the energy in the jet. In Section 4.2, we found that the time-scales and energy of the outflow are more easily explained by CNM-interactions from a single ejection of material around the time of the optical flare than a continuously-powered outflow, based on the small magnitude of the increasing energy compared to the

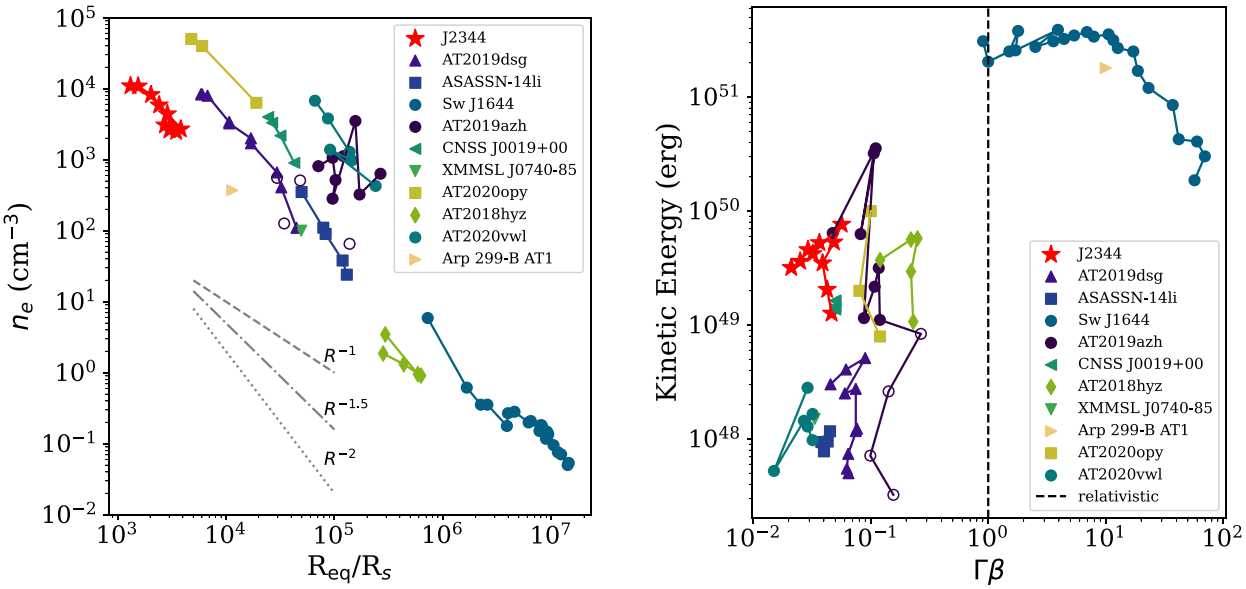

Figure 7. Left: The variation of ambient density with distance from the black hole for TDEs with well-sampled radio light curves as traced by outflow modelling. Right: The kinetic energy and velocity of the outflow produced in a selection of thermal TDEs. The equipartition-corrected estimated kinetic energy is plotted for J2344 for the spherical model. In both panels, J2344 is shown with red stars. J2344 appears to fit well into the population of non-relativistic TDEs in terms of energy, velocity, and ambient density (although the ambient density appears to be slightly lower than other events). TDE data and assumed SMBH masses are from Stein et al. (2021); Cendes et al. (2021b) (AT2019dsg, $M_{BH} = 5 \times 10^6$ M$_\odot$), Alexander et al. (2016) (ASASSN-14li, $M_{BH} = 1 \times 10^6$ M$_\odot$), Eftekhari et al. (2018) (Sw J1644 + 57, $M_{BH} = 1 \times 10^6$ M$_\odot$), Anderson et al. (2020) (CNSS J0019 + 00, $M_{BH} = 1 \times 10^7$ M$_\odot$), Mattila et al. (2018) (Arp 299-B AT1, $M_{BH} = 2 \times 10^7$ M$_\odot$), Alexander et al. (2017) (XMMSL1 J0740-85, $M_{BH} = 3.5 \times 10^6$ M$_\odot$), Goodwin et al. (2022) (AT2019azh, $M_{BH} = 3 \times 10^6$ M$_\odot$), Goodwin et al. (2023a) (AT2020opy, $M_{BH} = 1.12 \times 10^7$ M$_\odot$), Goodwin et al. (2023b) (AT2020vwl, $M_{BH} = 6.17 \times 10^5$ M$_\odot$). For J2344, we assume $M_{BH} = 6.3 \times 10^7$ M$_\odot$ (Homan et al. 2023).

expected accretion power that might power a jet. It therefore seems more likely that the transient emission observed from J2344 was due to a TDE in a LLAGN, as opposed to AGN activity in the galaxy.

6 CONCLUSIONS

We present 10 epochs of detailed radio spectral observations of a radio flare discovered from the nuclear transient J2344, which was temporally coincident with an optical, X-ray, UV, and infrared flare. Our radio observations enable us to track the outflow properties, such as radius, energy, velocity, and magnetic field strength over the 2.5 yrs spanned by our observations. We find that the radio flare is well explained by an expanding synchrotron-emitting region. Based on the energy and evolution time-scales of this outflow, we infer that it is more likely produced by a single ejection of material from the central SMBH than by a continuous ejection of energy into a jet from accretion.

The evolution time-scales, energetics, and luminosity of the radio flare are broadly consistent with the known non-relativistic radio-emitting TDE population. The radio luminosity of the radio emission from J2344 is among the brightest of the radio-detected TDEs to date, consistent with the high optical luminosity of the optical flare also associated with this event. In the TDE scenario, the outflow properties favour a spherical outflow launched by stream–stream collisions during the debris circularization or the unbound debris stream, but could also be explained by a mildly collimated jet launched from accretion onto the SMBH. We find no evidence of relativistic motion of the outflow.

The level of variability and time-scale of variability of the radio flare is also broadly consistent with AGN flares, but no previous flaring activity has been detected in the host galaxy over the past decade. Due to the outflow energetics requiring a single ejection of material, rather than the AGN-flare model of shock-in-jet, we conclude that it is more likely that the nuclear transient event was produced by a TDE in a switched off or low-luminosity AGN, but we cannot rule out a sudden accretion episode in a pre-existing switched off or low-luminosity AGN.

Future observations that continue to track the decay of the radio emission will enable the CNM density of the host galaxy to be measured further from the central SMBH as well as determining whether the decay of the radio emission behaves similar to other radio-detected TDEs. Longer time baseline monitoring campaigns to search for additional flares and to track the evolution of the source are ongoing and will be insightful in determining the true nature of this interesting transient event.

ACKNOWLEDGEMENTS

We thank the anonymous referee for their feedback, which helped to improve this manuscript. This work was supported by the Australian government through the Australian Research Council's Discovery Projects funding scheme (DP200102471). AM acknowledges support by DLR under the grant 50 QR 2110 (XMMNuTra). MK and DH acknowledge support from DLR grant FKZ 50 OR 2307 and FKZ 50 OR 2003, respectively. The Australia Telescope Compact Array is part of the Australia Telescope National Facility (https://ror.org/05qajvd42), which is funded by the Australian Government for operation as a National Facility managed by CSIRO. We acknowledge the Gomeroi people as the Traditional Owners of the Observatory site. We acknowledge ESA *Gaia*, DPAC, and the Photometric Science Alerts Team (http://gsaweb.ast.cam.ac.uk/alerts).

DATA AVAILABILITY

The radio data presented in Table A1 is available in machine readable format with the online publication of this work.

REFERENCES

Alexander K. D., Berger E., Guillochon J., Zauderer B. A., Williams P. K. G., 2016, ApJ, 819, L25
Alexander K. D., van Velzen S., Horesh A., Zauderer B. A., 2020, Space Sci. Rev., 216, 81
Alexander K. D., Wieringa M. H., Berger E., Saxton R. D., Komossa S., 2017, ApJ, 837, 153
Anderson G. E. et al., 2017, MNRAS, 466, 3648
Anderson M. M. et al., 2020, ApJ, 903, 116
Auchettl K., Ramirez-Ruiz E., Guillochon J., 2018, ApJ, 852, 37
Barniol Duran R., Nakar E., Piran T., 2013, ApJ, 772, 78
CASA Team et al., 2022, PASP, 134, 114501
Cendes Y. et al., 2022, ApJ, 938, 28
Cendes Y. et al., 2023, preprint (arXiv:2308.13595)
Cendes Y., Alexander K. D., Berger E., Eftekhari T., Williams P. K. G., Chornock R., 2021b, ApJ, 919, 127
Cendes Y., Eftekhari T., Berger E., Polisensky E., 2021a, ApJ, 908, 125
Chevalier R. A., 1982a, ApJ, 258, 790
Chevalier R. A., 1982b, ApJ, 259, 302
Chevalier R. A., 1998, ApJ, 499, 810
Ciotti L., Ostriker J. P., 2007, ApJ, 665, 1038
Cordes J. M., Lazio T. J. W., 2002, preprint(astro–ph/0207156)
Dai L., McKinney J. C., Roth N., Ramirez-Ruiz E., Miller M. C., 2018, ApJ, 859, L20
de Vries M., Kuijpers J., 1992, A&A, 266, 77
Donley J. L., Brandt W. N., Eracleous M., Boller T., 2002, AJ, 124, 1308
Eftekhari T., Berger E., Zauderer B. A., Margutti R., Alexander K. D., 2018, ApJ, 854, 86
Fabian A. C., 2012, ARA&A, 50, 455
Farrar G. R., Gruzinov A., 2009, ApJ, 693, 329
Fiore F. et al., 2017, A&A, 601, A143
Foreman-Mackey D., Hogg D. W., Lang D., Goodman J., 2013, PASP, 125, 306
Gaia Collaboration et al., 2016, A&A, 595, A1
Gezari S. et al., 2009, ApJ, 698, 1367
Goodwin A. J. et al., 2022, MNRAS, 511, 5328
Goodwin A. J. et al., 2023a, MNRAS, 518, 847
Goodwin A. J. et al., 2023b, MNRAS, 522, 5084
Granot J., Sari R., 2002, ApJ, 568, 820
Guillochon J., Ramirez-Ruiz E., 2013, ApJ, 767, 25
Guillochon J., Ramirez-Ruiz E., 2015, ApJ, 809, 166
Hale C. L. et al., 2021, PASA, 38, e058
Hammerstein E. et al., 2023, ApJ, 942, 9
Hills J. G., 1975, Nature, 254, 295
Homan D. et al., 2023, A&A, 672, A167
Horesh A. et al., 2013, MNRAS, 436, 1258
Horesh A., Cenko S. B., Arcavi I., 2021, Nat. Astron., 5, 491
Hovatta T., Nieppola E., Tornikoski M., Valtaoja E., Aller M. F., Aller H. D., 2008, A&A, 485, 51
Kajava J. J. E., Giustini M., Saxton R. D., Miniutti G., 2020, A&A, 639, A100
Komossa S., Bade N., 1999, A&A, 343, 775
Krolik J., Piran T., Svirski G., Cheng R. M., 2016, ApJ, 827, 127
Lightman A. P., Eardley D. M., 1974, ApJ, 187, L1
Liu Z. et al., 2023, A&A, 669, A75
Lodato G., King A. R., Pringle J. E., 2009, MNRAS, 392, 332
Lu W., Bonnerot C., 2020a, MNRAS, 492, 686
Lu W., Bonnerot C., 2020b, MNRAS, 492, 686
Malyali A. et al., 2023a, MNRAS, 520, 3549
Malyali A. et al., 2023b, MNRAS, 520, 4209
Marscher A. P., Gear W. K., 1985, ApJ, 298, 114
Matsumoto T., Piran T., 2023, MNRAS, 522, 4565
Matsumoto T., Piran T., Krolik J. H., 2022, MNRAS, 511, 5085
Mattila S. et al., 2018, Science, 361, 482
McConnell D. et al., 2020, PASA, 37, e048
Park J., Caprioli D., Spitkovsky A., 2015, Phys. Rev. Lett., 114, 085003
Pérez-Torres M. A., Alberdi A., Marcaide J. M., 2001, A&A, 374, 997
Phinney E. S., 1989, in Morris M., ed., The Center of the Galaxy. Vol. 136, Kluwer Academic Publishers, Dordrecht, p. 543
Predehl P. et al., 2021, A&A, 647, A1
Pyatunina T. B., Kudryavtseva N. A., Gabuzda D. C., Jorstad S. G., Aller M. F., Aller H. D., Teräsranta H., 2007, MNRAS, 381, 797
Ravi V. et al., 2022, ApJ, 925, 220
Rees M. J., 1984, ARA&A, 22, 471
Rees M. J., 1988, Nature, 333, 523
Ross K. et al., 2021, MNRAS, 501, 6139
Salas P., Bauer F. E., Stockdale C., Prieto J. L., 2013, MNRAS, 428, 1207
Saxton R., Komossa S., Auchettl K., Jonker P. G., 2020, Space Sci. Rev., 216, 85
Sironi L., Giannios D., 2013, ApJ, 778, 107
Sniegowska M., Czerny B., Bon E., Bon N., 2020, A&A, 641, A167
Soltan A., 1982, MNRAS, 200, 115
Somalwar J. J. et al., 2023, ApJ, 945, 142
Somalwar J. J., Ravi V., Dong D., Graham M., Hallinan G., Law C., Lu W., Myers S. T., 2022, ApJ, 929, 184
Spaulding A., Chang P., 2022, MNRAS, 515, 1699
Stein R. et al., 2021, Nat. Astron., 5, 510
Sunyaev R. et al., 2021, A&A, 656, A132
Truemper J., 1982, Adv. Space Res., 2, 241
Valtaoja E., Terasranta H., Urpo S., Nesterov N. S., Lainela M., Valtonen M., 1992a, A&A, 254, 71
Valtaoja E., Terasranta H., Urpo S., Nesterov N. S., Lainela M., Valtonen M., 1992b, A&A, 254, 80
van Velzen S., Holoien T. W. S., Onori F., Hung T., Arcavi I., 2020, Space Sci. Rev., 216, 124
van Velzen S., Pasham D. R., Komossa S., Yan L., Kara E. A., 2021, Space Sci. Rev., 217, 63
Walker M. A., 1998, MNRAS, 294, 307
Weiler K. W., Panagia N., Montes M. J., Sramek R. A., 2002, ARA&A, 40, 387
Weiler K. W., Sramek R. A., Panagia N., van der Hulst J. M., Salvati M., 1986, ApJ, 301, 790
Wevers T. et al., 2023, ApJ, 942, L33
Xu R., Spitkovsky A., Caprioli D., 2020, ApJ, 897, L41
Yao Y. et al., 2023, ApJ, 955, L6

SUPPORTING INFORMATION

Supplementary data are available at *MNRAS* online.

suppl_data

Please note: Oxford University Press is not responsible for the content or functionality of any supporting materials supplied by the authors. Any queries (other than missing material) should be directed to the corresponding author for the article.

APPENDIX A: RADIO FLUX DENSITY MEASUREMENTS

Table A1. ATCA flux density measurements of J2344. Both the statistical flux density error and additional error due to interstellar scintilaltion (ISS) are given.

Date (MJD)	Frequency (GHz)	Flux density ± statistical error ± ISS error (μJy)
59309	5.0	274 ± 11 ±82
59309	6.0	270 ± 19 ±81
59309	8.5	274 ± 20 ±27
59309	9.5	269 ± 16 ±27
59371	2.6	279 ± 23 ±126
59371	5.0	350 ± 13 ±105
59371	6.0	373 ± 11 ±112
59371	8.5	409 ± 16 ±41
59371	9.5	399 ± 11 ±40
59492	2.1	239 ± 45 ±108
59492	5.0	409 ± 23 ±123
59492	6.0	503 ± 20 ±151
59492	8.5	600 ± 45 ±60
59492	9.5	562 ± 26 ±56
59541	1.6	327 ± 53 ±147
59541	2.6	558 ± 50 ±251
59541	5.0	528 ± 25 ±158
59541	6.0	573 ± 21 ±172
59541	8.5	717 ± 24 ±72
59541	9.5	773 ± 24 ±77
59541	17.2	323 ± 35 ±0
59541	16.2	347 ± 26 ±0
59541	21.7	381 ± 44 ±0
59541	20.7	261 ± 55 ±0
59600	1.6	403 ± 30 ±181
59600	2.6	497 ± 32 ±224
59600	5.0	782 ± 37 ±235
59600	6.0	603 ± 25 ±181
59600	8.5	792 ± 31 ±79
59600	9.5	741 ± 31 ±74
59600	17.2	315 ± 25 ±0
59600	16.2	369 ± 27 ±0
59600	21.7	269 ± 60 ±0
59600	20.7	233 ± 22 ±0
59673	1.6	452 ± 59 ±204
59673	2.6	547 ± 101 ±246
59673	5.0	565 ± 26 ±169
59673	6.0	481 ± 45 ±144
59673	8.5	526 ± 43 ±53
59673	9.5	621 ± 154 ±62
59818	2.1	328 ± 64 ±148
59818	5.0	671 ± 21 ±201
59818	6.0	643 ± 17 ±193
59818	8.5	552 ± 14 ±55
59818	9.5	495 ± 14 ±49
59818	17.2	222 ± 15 ±0
59818	16.2	177 ± 18 ±0
59818	21.7	211 ± 30 ±0
59818	20.7	218 ± 23 ±0
59924	2.1	302 ± 50 ±136
59924	5.0	649 ± 25 ±195
59924	6.0	609 ± 18 ±183
59924	8.5	467 ± 16 ±47
59924	9.5	399 ± 18 ±40
59924	17.2	251 ± 32 ±0
59924	16.2	320 ± 31 ±0
59924	21.7	351 ± 80 ±0
59924	20.7	76 ± 19 ±0
60020	2.1	320 ± 184 ±144
60020	5.0	565 ± 67 ±169
60020	6.0	488 ± 33 ±146
60020	8.5	393 ± 24 ±39
60020	9.5	329 ± 22 ±33
60020	16.7	144 ± 24 ±0
60101	2.6	316 ± 44 ±142
60101	5.0	611 ± 22 ±183
60101	6.0	616 ± 20 ±185
60101	8.5	395 ± 19 ±40
60101	9.5	303 ± 18 ±30
60101	16.7	172 ± 18 ±0

APPENDIX B: OUTFLOW MODELS ASSUMING DIFFERENT DEVIATION FROM EQIUPARTITION

Table B1. Equipartition modelling properties of the outflow produced by J2344 based on the synchrotron spectral fits for different assumed deviation from equipartition, where ϵ_B is the fraction of energy in the magnetic field and ϵ_e is the fraction of energy carried by the electrons.

	Time (d)[1]	log R (cm)	log E (erg)	β	log B (G)	log n_e (cm^{-3})	log M_{ej} (g)
	$\epsilon_e = 10^{-3}$	$\epsilon_B = 0.02$					
	214	16.61 ± 0.13	50.73 ± 0.18	0.07 ± 0.02	0.83 ± 12.83	1.48 ± 1.23	32.33 ± 0.22
	276	16.68 ± 0.11	50.94 ± 0.17	0.07 ± 0.02	0.83 ± 10.78	1.48 ± 1.05	32.62 ± 0.20
	397	16.79 ± 0.14	51.17 ± 0.19	0.06 ± 0.02	0.77 ± 11.76	1.36 ± 1.30	32.92 ± 0.23
	446	16.95 ± 0.10	51.35 ± 0.16	0.08 ± 0.02	0.64 ± 6.20	1.08 ± 0.96	32.92 ± 0.19
Spherical	505	17.07 ± 0.11	51.51 ± 0.17	0.09 ± 0.02	0.53 ± 5.29	0.87 ± 1.04	32.95 ± 0.20
	578	16.87 ± 0.22	51.25 ± 0.25	0.05 ± 0.03	0.70 ± 15.82	1.21 ± 2.03	33.17 ± 0.33
	723	17.03 ± 0.13	51.35 ± 0.18	0.06 ± 0.02	0.51 ± 6.16	0.84 ± 1.24	33.16 ± 0.22
	829	16.99 ± 0.14	51.28 ± 0.19	0.05 ± 0.02	0.54 ± 7.35	0.90 ± 1.37	33.28 ± 0.24
	925	16.97 ± 0.25	51.18 ± 0.28	0.04 ± 0.02	0.52 ± 12.11	0.86 ± 2.33	33.31 ± 0.37
	1006	16.92 ± 0.16	51.13 ± 0.20	0.03 ± 0.01	0.56 ± 8.22	0.93 ± 1.48	33.41 ± 0.25
	214	16.99 ± 0.13	51.29 ± 0.18	0.16 ± 0.05	0.58 ± 7.13	0.97 ± 1.23	32.22 ± 0.22
	276	17.06 ± 0.11	51.50 ± 0.17	0.15 ± 0.04	0.58 ± 5.99	0.96 ± 1.05	32.50 ± 0.20
	397	17.17 ± 0.14	51.73 ± 0.19	0.14 ± 0.04	0.52 ± 6.53	0.84 ± 1.30	32.80 ± 0.23
	446	17.33 ± 0.10	51.91 ± 0.16	0.17 ± 0.04	0.38 ± 3.45	0.57 ± 0.96	32.81 ± 0.19
Conical	505	17.45 ± 0.11	52.07 ± 0.17	0.19 ± 0.05	0.27 ± 2.94	0.36 ± 1.04	32.86 ± 0.20
	578	17.25 ± 0.22	51.81 ± 0.25	0.12 ± 0.06	0.44 ± 8.79	0.70 ± 2.03	33.03 ± 0.33
	723	17.41 ± 0.13	51.91 ± 0.18	0.13 ± 0.04	0.26 ± 3.42	0.33 ± 1.24	33.03 ± 0.22
	829	17.36 ± 0.14	51.85 ± 0.19	0.11 ± 0.04	0.29 ± 4.09	0.39 ± 1.37	33.14 ± 0.24
	925	17.34 ± 0.25	51.75 ± 0.28	0.09 ± 0.05	0.27 ± 6.73	0.35 ± 2.33	33.16 ± 0.37
	1006	17.30 ± 0.16	51.69 ± 0.20	0.08 ± 0.03	0.30 ± 4.57	0.42 ± 1.48	33.25 ± 0.25
	250	16.99 ± 0.13	51.29 ± 0.18	0.14 ± 0.04	0.58 ± 7.13	0.97 ± 1.23	32.34 ± 0.22
	312	17.06 ± 0.11	51.50 ± 0.17	0.13 ± 0.03	0.58 ± 5.99	0.96 ± 1.05	32.59 ± 0.20
	433	17.17 ± 0.14	51.73 ± 0.19	0.13 ± 0.04	0.52 ± 6.53	0.84 ± 1.30	32.87 ± 0.23
	482	17.33 ± 0.10	51.91 ± 0.16	0.16 ± 0.04	0.38 ± 3.45	0.57 ± 0.96	32.87 ± 0.19
	541	17.45 ± 0.11	52.07 ± 0.17	0.18 ± 0.05	0.27 ± 2.94	0.36 ± 1.04	32.90 ± 0.20
	614	17.25 ± 0.22	51.81 ± 0.25	0.11 ± 0.05	0.44 ± 8.79	0.70 ± 2.03	33.08 ± 0.33
	759	17.41 ± 0.13	51.91 ± 0.18	0.12 ± 0.04	0.26 ± 3.42	0.33 ± 1.24	33.07 ± 0.22
	865	17.36 ± 0.14	51.85 ± 0.19	0.10 ± 0.03	0.29 ± 4.09	0.39 ± 1.37	33.18 ± 0.24
	961	17.34 ± 0.25	51.75 ± 0.28	0.09 ± 0.05	0.27 ± 6.73	0.35 ± 2.33	33.19 ± 0.37
	1042	17.30 ± 0.16	51.69 ± 0.20	0.08 ± 0.03	0.30 ± 4.57	0.42 ± 1.48	33.28 ± 0.25
	$\epsilon_e = 10^{-4}$	$\epsilon_B = 0.02$					
	214	16.72 ± 0.13	51.91 ± 0.18	0.09 ± 0.03	1.27 ± 35.09	0.19 ± 1.23	33.32 ± 0.22
	276	16.79 ± 0.11	52.12 ± 0.17	0.09 ± 0.02	1.27 ± 29.48	0.18 ± 1.05	33.60 ± 0.20
	397	16.90 ± 0.14	52.35 ± 0.19	0.08 ± 0.02	1.21 ± 32.17	0.06 ± 1.30	33.90 ± 0.23
	446	17.06 ± 0.10	52.53 ± 0.16	0.10 ± 0.02	1.07 ± 16.97	−0.21 ± 0.96	33.90 ± 0.19
Spherical	505	17.18 ± 0.11	52.69 ± 0.17	0.11 ± 0.03	0.97 ± 14.47	−0.42 ± 1.04	33.94 ± 0.20
	578	16.98 ± 0.22	52.43 ± 0.25	0.07 ± 0.03	1.14 ± 43.27	−0.08 ± 2.03	34.15 ± 0.33
	723	17.14 ± 0.13	52.53 ± 0.18	0.07 ± 0.02	0.95 ± 16.86	−0.45 ± 1.24	34.13 ± 0.22
	829	17.09 ± 0.14	52.47 ± 0.19	0.06 ± 0.02	0.98 ± 20.12	−0.39 ± 1.37	34.26 ± 0.24
	925	17.07 ± 0.25	52.37 ± 0.28	0.05 ± 0.03	0.96 ± 33.14	−0.43 ± 2.33	34.29 ± 0.37
	1006	17.03 ± 0.16	52.31 ± 0.20	0.04 ± 0.02	1.00 ± 22.48	−0.36 ± 1.48	34.38 ± 0.25
	214	17.09 ± 0.13	52.47 ± 0.18	0.20 ± 0.06	1.02 ± 19.50	−0.32 ± 1.23	33.23 ± 0.22
	276	17.17 ± 0.11	52.68 ± 0.17	0.18 ± 0.05	1.01 ± 16.38	−0.33 ± 1.05	33.50 ± 0.20
	397	17.28 ± 0.14	52.91 ± 0.19	0.17 ± 0.05	0.95 ± 17.87	−0.45 ± 1.30	33.80 ± 0.23
	446	17.43 ± 0.10	53.10 ± 0.16	0.21 ± 0.05	0.82 ± 9.43	−0.72 ± 0.96	33.82 ± 0.19
Conical	505	17.56 ± 0.11	53.25 ± 0.17	0.23 ± 0.06	0.71 ± 8.04	−0.93 ± 1.04	33.87 ± 0.20
	578	17.36 ± 0.22	53.00 ± 0.25	0.14 ± 0.07	0.88 ± 24.04	−0.59 ± 2.03	34.03 ± 0.33
	723	17.51 ± 0.13	53.09 ± 0.18	0.16 ± 0.05	0.69 ± 9.36	−0.97 ± 1.24	34.02 ± 0.22
	829	17.47 ± 0.14	53.03 ± 0.19	0.13 ± 0.04	0.73 ± 11.18	−0.90 ± 1.37	34.13 ± 0.24
	925	17.45 ± 0.25	52.93 ± 0.28	0.12 ± 0.07	0.70 ± 18.41	−0.94 ± 2.33	34.15 ± 0.37
	1006	17.41 ± 0.16	52.87 ± 0.20	0.10 ± 0.04	0.74 ± 12.49	−0.87 ± 1.48	34.24 ± 0.25

[1]Measured with respect to the optical flare date, MJD 59095.3

This paper has been typeset from a TEX/LATEX file prepared by the author.